Vision-Based Safety-Critical Landing Control of Quadrotors With External Uncertainties and Collision Avoidance

Jie Lin, Zhiqiang Miao, *Member, IEEE*, Yaonan Wang, Hesheng Wang, *Senior Member, IEEE*, Xiangke Wang, and Rafael Fierro, *Senior Member, IEEE*

***Abstract*— This article addresses the quadrotors' safety-critical landing control problem with external uncertainties and collision avoidance. A geometrically robust hierarchical control strategy is proposed for an underactuated quadrotor, which consists of a slow outer loop controlling the position and a fast inner loop regulating the attitude. First, an estimation error quantified (EEQ) observer is developed to identify and compensate for the target's linear acceleration and the translational disturbances, whose estimation error has a nonnegative upper bound. Furthermore, an outer-loop controller is designed by embedding the EEQ observer and control barrier functions (CBFs), in which the negative effects of external uncertainties, collision avoidance, and input saturation are thoroughly considered and effectively attenuated. For the inner-loop subsystem, a geometric controller with a robust integral of the sign of the error (RISE) control structure is developed to achieve disturbances rejection and asymptotic attitude tracking. Based on Lyapunov techniques and the theory of cascade systems, it is rigorously proven that the closed-loop system is uniformly ultimately bounded. Finally, the effectiveness of the proposed control strategy is demonstrated through numerical simulations and hardware experiments.**

***Index Terms*— Collision avoidance, disturbance rejection, landing control, position-based visual servoing (PBVS), quadrotor.**

I. Introduction

UNMANNED aerial vehicles (UAVs) have received considerable attention from the research community in recent years due to their potential in various military and civilian applications, such as exploration [1], search and rescue [2], and surveillance [3]. As a necessary task to deploy and recover UAVs, safety-critical landing aims to achieve stable tracking while ensuring collision avoidance constraints. Of particular interest are quadrotors due to their special superiorities (e.g., simple structure, rapid maneuverability, and vertical take-off and landing) and their potential applications in complex environments [4], [5]. As quadrotors grow in power and maneuverability, their low inertia renders them quadrotor-susceptible to external disturbances and motion collisions, which creates an even greater challenge to the design of safe landing controllers for quadrotors. Therefore, safe landing control of quadrotors with external uncertainties and collision avoidance is crucial in practice.

To be reactive to indoor and outdoor environments and possess sufficient local accuracy for landing, instead of the Global Positioning System (GPS), the use of onboard cameras has become a fundamental necessity for quadrotors. Visual servoing can be classified into image-based visual servoing (IBVS) and position-based visual servoing (PBVS). The IBVS method directly uses image features to regulate the motion of the quadrotor [6], [7], [8]. However, it introduces a highly coupled image Jacobian and may produce undesired motion trajectories in Cartesian space. In contrast, the mechanism of the PBVS method is to reconstruct the pose information from 2-D image data. Therefore, PBVS has the advantage of separating the controller design problem from the vision-based state estimation problem, as illustrated in [9], [10], and [11]. The level of the quadrotor's maneuverability is closely related to the attitude representation methods, which can be roughly grouped into three categories: Euler angles [12], quaternions [13], or rotation matrices [14]. In the Euler angle attitude representation method, there are mathematical singularities called "gimbal lock." Quaternions are ambiguous in representing an attitude. Therefore, geometric attitude controllers have been developed to use rotation matrices directly to achieve a singularity-free attitude representation.

To avoid collision problems during the landing of inherently unstable quadrotor systems, several safe control approaches have been studied. Model predictive control (MPC) is a typical finite-horizon control method using an optimization framework to handle constraints on input and state variables simultaneously. In [15], the collision avoidance constraints were implemented based on a sigmoid function. In [16], the general

Manuscript received 27 September 2022; revised 31 July 2023 and 22 November 2023; accepted 4 February 2024. Date of publication 14 February 2024; date of current version 25 June 2024. This work was supported in part by the National Key Research and Development Program of China under Grant 2022YFB3903804, in part by the Natural Science Foundation of China under Grant 62273138, in part by the Science and Technology Innovation Program of Hunan Province under Grant 2021RC3060, and in part by the Postgraduate Scientific Research Innovation Project of Hunan Province under Grant QL20210080. Recommended by Associate Editor C. Edwards. *(Corresponding author: Zhiqiang Miao.)*

Jie Lin, Zhiqiang Miao, and Yaonan Wang are with the College of Electrical and Information Engineering, Hunan University, Changsha 410082, China, and also with the National Engineering Laboratory for Robot Visual Perception and Control, Changsha 410073, China (e-mail: linjie0275@hnu.edu.cn; miaozhiqiang@hnu.edu.cn; yaonan@hnu.edu.cn).

Hesheng Wang is with the Department of Automation and the Key Laboratory of System Control and Information Processing, Ministry of Education of China, Shanghai Jiao Tong University, Shanghai 200240, China, and also with the State Key Laboratory of Robotics and System, Harbin Institute of Technology, Harbin 150001, China (e-mail: wanghesheng@sjtu.edu.cn).

Xiangke Wang is with the College of Intelligence Science and Technology, National University of Defense Technology, Changsha 410073, China (e-mail: xkwang@nudt.edu.cn).

Rafael Fierro is with the MARHES Laboratory, Department of Electrical and Computer Engineering, University of New Mexico, Albuquerque, NM 87131 USA (e-mail: rfierro@unm.edu).

Digital Object Identifier 10.1109/TCST.2024.3363372

optimization is simplified into a convex optimization problem to apply MPC in real-time. In [17], a nonlinear MPC (NMPC) was proposed to track the desired trajectory while avoiding obstacles. Although MPC is handy in addressing different types of constraints, it consumes a lot of computing resources and might lead to unsafe operations for low-cost quadrotor systems. In [18], the artificial potential field (APF) method was extended and applied to quadrotors. Alternatively, control barrier functions (CBFs) are lightweight and efficient tools for converting the safety constraints into state-dependent linear inequality constraints on the inputs. Hence, the CBF-based quadratic program (CBF-QP) has become a powerful method to enforce safety constraints in the form of set invariance. In [19], CBF-QP was first implemented in adaptive cruise control to permit dynamically feasible constraints and ensure forward invariance. The case of collision avoidance for teams of quadrotors was studied in [20]. In [21], CBF constraints were imposed on the outer and inner loops of the controller to allow independent safety regulation in the quadrotor's altitude and lateral states. In [22] and [23], the safety-critical control framework was extended to quadrotors. The common idea of these works is to determine an appropriate control function such that the forward invariance of the safe set is guaranteed. Nonetheless, almost all of the aforementioned studies rely on precise mathematical models, which are typically difficult to obtain.

This is a challenging problem since quadrotors are susceptible to external uncertainties, such as friction, wind gusts, various payloads, and unknown targets. To this end, some robust CBF approaches have been proposed for quadrotor systems with external uncertainties. In [24], a learning-based CBF was presented for partially known systems based on Gaussian process regression. The case with uncertain nonlinear quadrotor dynamics was presented in [25]. The case for the tracking problem of quadrotors with wind disturbances was studied in [26]. However, this typically requires large amounts of quality data for the multirotor system. In [27], robust CBFs were proposed and combined with input-to-state stability control Lyapunov functions (ISS-CLFs) for constrained nonlinear systems with disturbances. The case with bounded state-estimation errors was considered in [28]. In [29], optimal robust control was developed for hybrid systems with model uncertainties. Although these state-of-the-art approaches have achieved some interesting results, they rely on the boundedness of uncertainties or the Lipschitzness of the unknown dynamics, which sacrifices the landing performance of the quadrotor to achieve better robustness.

In this article, we intend to solve the problem of vision-based safe landing control of quadrotors in the presence of external uncertainties and collision avoidance. Inspired by the estimation error quantization (EEQ) observer in [30], an EEQ observer is designed to estimate the external uncertainties such as the disturbance on the side of the quadrotor and the unknown target acceleration, as well as guaranteeing the estimated error with a nonnegative upper bound. Furthermore, an EEQ observer-based CBF scheme is proposed to achieve robust landing performance and intervehicle distance constraints. A geometric attitude controller is developed to represent attitude uniquely and achieve asymptotic stability. Compared with the available vision-based landing control schemes, the main contributions of this article are threefold.

1) A safety-critical PBVS control scheme is proposed to ensure collision avoidance while handling uncertain targets and disturbances. However, in PBVS landing methods [9], [10], [11] and robust CBF approaches [24], [25], [26], [27], [28], [29], the intervehicle distance constraints were not considered. Compared with the APF method in [18], the proposed method offers smooth landing behavior while avoiding collision at a lower energy cost. In contrast to collision avoidance approaches in [19], [20], [21], [22], and [23], the designed safe landing framework integrates CBF and EEQ observers, and the negative effects of external uncertainties, collision avoidance, and input saturation are fully considered and effectively attenuated.
2) An EEQ observer-based CBF scheme is formulated to achieve collision avoidance and compensate for external uncertainties within a quantitative estimation error bound. While in [29], the CBF constraints rely on a prior bound of the disturbance estimation error, which renders the control performance unnecessarily conservative. More significantly, the CBF constraints implemented in the quadrotors are low-complexity and real-time only considering the altitude constraints for 3-D ground targets.
3) Different from the classic geometric control method in [14], the proposed geometric controller is developed with a continuous robust integral of the sign of the error (RISE) control structure, which can compensate for external attitude disturbances and achieve asymptotic attitude tracking.

The rest of this article is organized as follows. Section II describes the quadrotor dynamics and the visual dynamics. In Section III, the design of the robust control scheme is presented, followed by the analysis of closed-loop stability. Numerical simulations and experimental results are shown in Section IV. Finally, Section V concludes this article.

II. Problem Formulation

A. Preliminaries

In this section, the notations and operators in Lie algebra are introduced. Denote the special orthogonal group SO(3) as

$$\mathrm{SO}(3) = \left\{ \boldsymbol{R} \in \mathbb{R}^{3\times 3} : \boldsymbol{R}^T \boldsymbol{R} = \boldsymbol{R}\boldsymbol{R}^T = I_3, \det(\boldsymbol{R}) = 1 \right\}.$$

Its associated Lie algebra $\mathfrak{so}(3)$ is the real vector space of 3×3 skew-symmetric matrices as

$$\mathfrak{so}(3) = \left\{ \boldsymbol{B} \in \mathbb{R}^{3\times 3} : \boldsymbol{B} = -\boldsymbol{B}^T \right\}.$$

The isomorphism operator $(\cdot)^\wedge : \mathbb{R}^3 \mapsto \mathfrak{so}(3)$ is defined such that $(\boldsymbol{x})^\wedge \boldsymbol{y} = \boldsymbol{x} \times \boldsymbol{y}$ for all $\boldsymbol{x}, \boldsymbol{y} \in \mathbb{R}^3$, where $\times$ denotes the cross product. The inverse of $(\cdot)^\wedge : \mathfrak{so}(3) \mapsto \mathbb{R}^3$ is denoted by $(\cdot)^\vee$. For $\forall \boldsymbol{x} \in \mathbb{R}^3$ and $\boldsymbol{B} \in \mathfrak{so}(3)$, we have $((\boldsymbol{x})^\wedge)^\vee = \boldsymbol{x}$ and $((\boldsymbol{B})^\wedge)^\vee = \boldsymbol{B}$. The Euclidean norm of a matrix is denoted

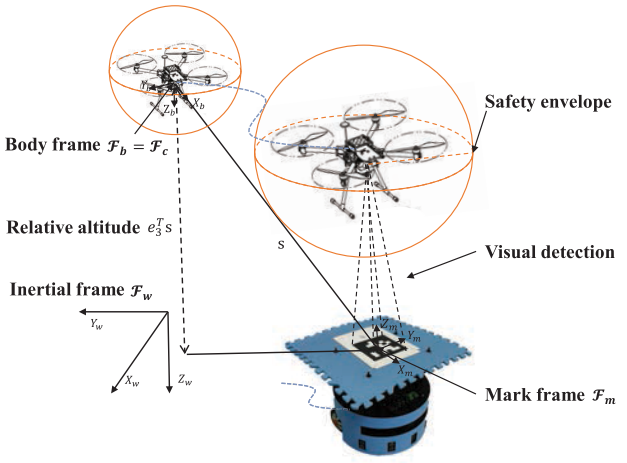

Fig. 1. Vision-based landing system and involved coordinate frames.

by $\|\cdot\|$. The principle matrix logarithm $\mathrm{Log}(\cdot)$ represents the inverse map from SO(3) to $\mathfrak{so}(3)$ and is defined as follows:

$$\mathrm{Log}(\boldsymbol{R}) = \frac{\varsigma}{2\sin(\varsigma)}\left(\boldsymbol{R} - \boldsymbol{R}^T\right)^{\vee}$$
$$\varsigma = \cos^{-1}\left(\frac{\mathrm{tr}(\boldsymbol{R}) - 1}{2}\right) \tag{1}$$

with $\mathrm{tr}(\cdot)$ denoting the trace of a matrix and $\|\varsigma\| \leq \pi$.

Lemma 1 [31]: Consider a system $\dot{\boldsymbol{x}} = f(\boldsymbol{x})$ and a defined set $\mathcal{L} = \{\boldsymbol{x} \in \mathbb{R}^n \mid h(\boldsymbol{x}) \geq 0\}$, if the following inequality holds:

$$\dot{h}(\boldsymbol{x}) \geq -\kappa_1(h(\boldsymbol{x})) \quad \forall \boldsymbol{x} \in \mathcal{N} \tag{2}$$

then the set $\mathcal{L}$ is forward invariant, where the function $h : \mathbb{R}^n \to \mathbb{R}$ named as the CBF is continuously differentiable, $\kappa_1(\cdot)$ is a locally Lipschitz extended class κ function, and $\mathcal{L} \subseteq \mathcal{N} \subset \mathbb{R}^n$.

Proposition 1: Consider a system $\dot{\boldsymbol{x}} = f(\boldsymbol{x})$ and a defined set $\mathcal{L} = \{\boldsymbol{x} \in \mathbb{R}^n \mid h(\boldsymbol{x}) \geq 0\}$, if the following inequality holds:

$$\dot{H}(\boldsymbol{x}) \geq -\kappa_2(H(\boldsymbol{x})) \quad \forall \boldsymbol{x} \in \mathcal{N} \tag{3}$$

then the set $\mathcal{L}$ is forward invariant, where the function $H = \dot{h}(\boldsymbol{x}) + \kappa_1(h(\boldsymbol{x}))$ is named as an extended zeroing barrier function, and $\kappa_1(\cdot)$ and $\kappa_2(\cdot)$ are a locally Lipschitz extended class κ functions.

Proof: According to Lemma 1, it can be proved with ease that the set $\mathcal{L}^* = \{\boldsymbol{x} \in \mathbb{R}^n \mid H(\boldsymbol{x}) \geq 0\}$ is forward invariant, that is, $\dot{h}(\boldsymbol{x}) \geq -\kappa_1(h(\boldsymbol{x}))$ always holds. Thus, the set $\mathcal{L} \subseteq \mathcal{N} \subset \mathbb{R}^n$ is also forward invariant. □

B. Quadrotor Dynamics

The coordinate system of the vision-based safe-critical landing of a quadrotor on a moving target is shown in Fig. 1. The quadrotor is equipped with an onboard downward camera to detect a moving unknown target with a visual mark. Let $\mathcal{F}_w = \{X_w, Y_w, Z_w\}$ represent a right-hand inertial reference frame, with Z_w being the vertical direction toward the ground, and $\mathcal{F}_b = \{X_b, Y_b, Z_b\}$ be a body-fixed frame, which is located at the center of mass of the quadrotor. For simplicity, it is assumed that the camera frame $\mathcal{F}_c = \{X_c, Y_c, Z_c\}$ is coincident with $\mathcal{F}_b$. To release this assumption, $\mathcal{F}_c$ and $\mathcal{F}_b$ can be related by a constant translation transformation. The rotation matrix from $\mathcal{F}_b$ to $\mathcal{F}_w$ is represented by $\boldsymbol{R} \in \mathbb{R}^{3\times3}$, it is associated with the three Euler angles φ, θ, ψ, which are the pitch angle (around the y-axis), the roll angle (around the x-axis), and the yaw angle (around the z-axis), respectively.

Let $\boldsymbol{p} \in \mathbb{R}^3$ and $\boldsymbol{v} \in \mathbb{R}^3$ denote the position and linear velocity of the quadrotor with respect to $\mathcal{F}_w$, and $\boldsymbol{\Omega} \in \mathbb{R}^3$ be the angular velocity expressed in $\mathcal{F}_b$. According to the mechanics of rigid body rotation and Newton–Euler formulation, the dynamics model of the quadrotor can be derived as

$$\dot{\boldsymbol{p}} = \boldsymbol{v} \tag{4a}$$
$$\dot{\boldsymbol{v}} = -\frac{f\boldsymbol{R}\boldsymbol{e}_3}{m} + g\boldsymbol{e}_3 + \boldsymbol{d}_f \tag{4b}$$
$$\dot{\boldsymbol{R}} = \boldsymbol{R}\boldsymbol{\Omega}^{\wedge} \tag{4c}$$
$$\boldsymbol{J}\dot{\boldsymbol{\Omega}} = \boldsymbol{\tau} - \boldsymbol{\Omega} \times \boldsymbol{J}\boldsymbol{\Omega} + \boldsymbol{d}_\tau \tag{4d}$$

where the physical properties of the quadrotor are defined by the total mass m, gravity acceleration g, and constant symmetric inertia matrix $\boldsymbol{J} \in \mathbb{R}^{3\times3}$, and the constant vector $\boldsymbol{e}_3 = [0, 0, 1]^T$. The four identical rotors and propellers are located at the vertices of a square, which generate a thrust $f \in \mathbb{R}$ and torque $\tau \in \mathbb{R}^3$ normal to the plane of this square. The external disturbances in the position and attitude loop are denoted as $\boldsymbol{d}_f \in \mathbb{R}^3$ and $\boldsymbol{d}_\tau \in \mathbb{R}^3$.

C. Vision-Based Position Estimation and Visual Dynamics

In this work, a PBVS is selected, with a downward camera mounted on the quadrotor facing the target of interest. There are different families of markers that have been developed for target landing, with circular and square shapes [32]. Circular markers provide accurate attitude estimation at short distances but are computationally expensive. In contrast, squared reference tags have lower computational costs, such as ARTags, ArUco, CCTag, ChromaTag, LFTag, AprilTags, and AprilTag2. Among them, AprilTag2 is a stronger digital coding system and has greater robustness to occlusion, warping, and lens distortion [33]. Therefore, a vision-based localization system is built using the AprilTag2 and a monocular camera.

For an AprilTag2 mark, the 3-D position of the square corner of the AprilTag2 can be denoted as $\boldsymbol{P}^m = [X_m, Y_m, Z_m]^T$ in its body frame $\mathcal{F}_m$. According to the camera pin-hole model, the transformation from the mark frame to the image coordinate system in pixels $[u, v]^T$ is given by

$$\lambda_c \begin{bmatrix} u \\ v \\ 1 \end{bmatrix} = \boldsymbol{M} \begin{bmatrix} \boldsymbol{R}_M^C & \boldsymbol{t}_M^C \\ \boldsymbol{0}^T & 1 \end{bmatrix} \begin{bmatrix} X_m \\ Y_m \\ Z_m \\ 1 \end{bmatrix} \tag{5}$$

with

$$\boldsymbol{M} = \begin{bmatrix} \alpha_x & 0 & u_0 & 0 \\ 0 & \alpha_y & v_0 & 0 \\ 0 & 0 & 1 & 0 \end{bmatrix}$$

where λ_c is the scaling factor, $\boldsymbol{M}$ is the camera intrinsic matrix with α_x, α_y, u_0, and v_0 determined by camera calibration, and $\boldsymbol{R}_M^C \in SO(3)$ and $\boldsymbol{t}_M^C \in \mathbb{R}^3$ represent the rotation and

translation of $\mathcal{F}_m$ relative to $\mathcal{F}_c$, respectively. Using (5), $\boldsymbol{R}_M^C \in SO(3)$ and $\boldsymbol{t}_M^C \in \mathbb{R}^3$ can be estimated based on the four square corners of the AprilTag and responding image points. The side length of the AprilTag is the only scale information.

The relative position between the quadrotor and the AprilTag center can be obtained by

$$\boldsymbol{s} = \boldsymbol{p} - \boldsymbol{p}_t = -\boldsymbol{R}\boldsymbol{R}_C^B \boldsymbol{t}_M^C \tag{6}$$

where $\boldsymbol{p}_t$ is the position of the AprilTag center expressed in $\mathcal{F}_w$, and $\boldsymbol{R}_C^B$ is a known fixed rotational transformation from the camera frame relative to the quadrotor body frame.

Now the visual dynamics is deduced as

$$\begin{aligned} \dot{\boldsymbol{s}} &= \boldsymbol{v} - \boldsymbol{v}_t \\ \dot{\boldsymbol{e}}_v &= \underbrace{\boldsymbol{U} - \boldsymbol{\chi}}_{-(f/m)\boldsymbol{R}\boldsymbol{e}_3} + g\boldsymbol{e}_3 + \boldsymbol{\eta}_f \end{aligned} \tag{7}$$

where $\boldsymbol{v}_t$ is the target's linear velocity, $\boldsymbol{e}_v = \boldsymbol{v} - \boldsymbol{v}_t$, and $\boldsymbol{\eta}_f = -\dot{\boldsymbol{v}}_t + \boldsymbol{d}_f$ is an integrated disturbance. The intermediary control input $\boldsymbol{U}$ and the coupling term $\boldsymbol{\chi}$ between the outer loop and the inner loop are given by

$$\boldsymbol{\chi} = \frac{f}{m\boldsymbol{e}_3^T \boldsymbol{R}_d^T \boldsymbol{R}\boldsymbol{e}_3}\left(\left(\boldsymbol{e}_3^T \boldsymbol{R}_d^T \boldsymbol{R}\boldsymbol{e}_3\right)\boldsymbol{R}\boldsymbol{e}_3 - \boldsymbol{R}_d\boldsymbol{e}_3\right) \tag{8}$$

$$\boldsymbol{U} = -\frac{f}{m\boldsymbol{e}_3^T \boldsymbol{R}_d^T \boldsymbol{R}\boldsymbol{e}_3}\boldsymbol{R}_d\boldsymbol{e}_3 \tag{9}$$

where $\boldsymbol{R}_d$ is the desired attitude command and will be illustrated in detail in Section III-C.

The quadrotor is a naturally unstable system with inherently nonlinear underactuated coupled dynamics, which creates difficulties for the control algorithm development. Typically, using the hierarchical control paradigm, the PBVS system can be divided into an outer-loop (slow time scale) subsystem (10) and an inner-loop (fast time scale) subsystem (11) as follows:

$$\begin{cases} \dot{\boldsymbol{s}} = \boldsymbol{e}_v \\ \dot{\boldsymbol{e}}_v = \boldsymbol{U} + g\boldsymbol{e}_3 + \boldsymbol{\eta}_f \end{cases} \tag{10}$$

and

$$\begin{cases} \dot{\boldsymbol{R}} = \boldsymbol{R}\boldsymbol{\Omega}^{\wedge} \\ \boldsymbol{J}\dot{\boldsymbol{\Omega}} = \boldsymbol{\tau} - \boldsymbol{\Omega} \times \boldsymbol{J}\boldsymbol{\Omega} + \boldsymbol{d}_\tau. \end{cases} \tag{11}$$

The translational subsystem (10) is regarded as a nominal subsystem without the coupling term χ in (7). Although the time-scale separation between the translational dynamics and the attitude dynamics can be considered for control design, the stability must be analyzed for the whole closed-loop system.

Instead of obtaining the prior target model and operating in ideal environments, some assumptions regarding the setup and the environment are established.

Assumption 1: The relative linear velocity $\boldsymbol{e}_v$ is assumed to be available by measuring the optical flow of the visual mark.

Assumption 2: The translational perturbation $\boldsymbol{\eta}_f$ and the rotational disturbance $\boldsymbol{d}_\tau$ are all bounded. There exists positive constants $\bar{\eta}_{f1} > 0$, $\bar{\eta}_{f2} > 0$, $\bar{d}_{\tau 1} > 0$, and $\bar{d}_{\tau 2} > 0$ such that $\|\boldsymbol{\eta}_f\| \le \bar{\eta}_{f1}$, $\|\dot{\boldsymbol{\eta}}_f\| \le \bar{\eta}_{f2}$, $\|\boldsymbol{d}_\tau\| \le \bar{d}_{\tau 1}$, $\|\dot{\boldsymbol{d}}_\tau\| \le \bar{d}_{\tau 2}$.

Note that, external uncertainties $\boldsymbol{\eta}_f$ and $\boldsymbol{d}_\tau$ are mainly generated by wind or other loads. Therefore, Assumption 2 is reasonable in practice.

Remark 1: To improve the accuracy and robustness of pose estimation, a Kalman filter can be adapted to the entire process. Using the constant-velocity model [34], the prediction and update parts are given as follows:

$$\begin{aligned} \hat{\boldsymbol{X}}_{k,k-1} &= \Phi\hat{\boldsymbol{X}}_{k-1,k-1} \\ \boldsymbol{P}_{k,k-1} &= \Phi\boldsymbol{P}_{k-1,k-1}\Phi^T + \Gamma\boldsymbol{Q}_{k-1,k-1}\Gamma^T \\ \boldsymbol{K}_k &= \boldsymbol{P}_{k,k-1}\boldsymbol{H}^T\left(\boldsymbol{H}\boldsymbol{P}_{k,k-1}\boldsymbol{H}^T + \boldsymbol{O}_k\right)^{-1} \\ \hat{\boldsymbol{X}}_{k,k} &= \hat{\boldsymbol{X}}_{k,k-1} + \boldsymbol{K}_k\left(\boldsymbol{Z}_k - \boldsymbol{H}\hat{\boldsymbol{X}}_{k,k-1}\right) \\ \boldsymbol{P}_{k,k} &= (\boldsymbol{I} - \boldsymbol{K}_k\boldsymbol{H})\boldsymbol{P}_{k,k-1} \end{aligned}$$

with

$$\Phi = \begin{bmatrix} \boldsymbol{I}_{3\times3} & T_s \cdot \boldsymbol{I}_{3\times3} \\ \boldsymbol{0}_{3\times3} & \boldsymbol{I}_{3\times3} \end{bmatrix}, \quad \Gamma = \begin{bmatrix} \boldsymbol{0}_{3\times3} & \boldsymbol{0}_{3\times3} \\ \boldsymbol{0}_{3\times3} & \boldsymbol{I}_{3\times3} \end{bmatrix}$$

where $\boldsymbol{X}_k = [\boldsymbol{s}^T, \boldsymbol{e}_v^T]^T$, $\boldsymbol{H} = [\boldsymbol{I}_{3\times3}, \boldsymbol{0}_{3\times3}]$, $\boldsymbol{Z}_k = \boldsymbol{H}\boldsymbol{X}_k$. T_s is the sampling period. $\boldsymbol{P}_{k,k-1}$ and $\boldsymbol{P}_{k,k}$ represent the prior and posterior covariance of the estimation error, respectively. $\boldsymbol{K}_k$ denotes the Kalman gain matrix at step k. $\boldsymbol{Q}_{k,k-1}$ represents the covariance of the systematic noise and $\boldsymbol{O}_k$ denotes the covariance of the observation noise. By implementing this Kalman filter, a more reliable state is given by $\boldsymbol{s} = \boldsymbol{H}\hat{\boldsymbol{X}}_{k,k}$.

As a prerequisite to implementing PBVS for the quadrotor, the ground target should be within the field of view of the camera. In practical engineering applications, the AprilTag has shown the ability to handle partial occlusions and temporary loss. In contrast to traditional simultaneous localization and mapping (SLAM) scenarios, where the camera or sensor typically conducts feature extraction on key frames to ascertain the scene's structure and the camera's motion throughout the entire process, the AprilTag 2 algorithm utilized in this study performs real-time tag detection and pose estimation for each frame of the video stream. Its low computational complexity eliminates the necessity for key frames. Once the current relative position is obtained, quadrotors can quickly recover tracking maneuverability. Note that the novelty of this article does not lie in proposing a new localization algorithm but rather in designing a safety landing controller. Hence, the different markers only provide localization information and do not affect the performance of the proposed landing framework.

D. Problem Statement

The objective of this article is to design a safety-critical PBVS scheme for a low-cost quadrotor to achieve collision avoidance and uncertainty rejection during landing. Since it is impractical to obtain the motion parameters of an unknown moving target in advance, the relative position and velocity between the quadrotor and the target can be provided by using a monocular camera and measuring the optical flow [8], respectively. The attitude angles and angular velocities of the quadrotor are provided by an inertial measurement unit (IMU). The smallest collision avoidance radii γ can be set based on the wheelbase of the quadrotor.

Specifically, given a desired tracking position deviation $\boldsymbol{s}_d$, the control objective here is to design the thrust force f and torque input $\boldsymbol{\tau}$ for the quadrotor to converge the relative position $\boldsymbol{s}$ to the desired value $\boldsymbol{s}_d$ with external uncertainties

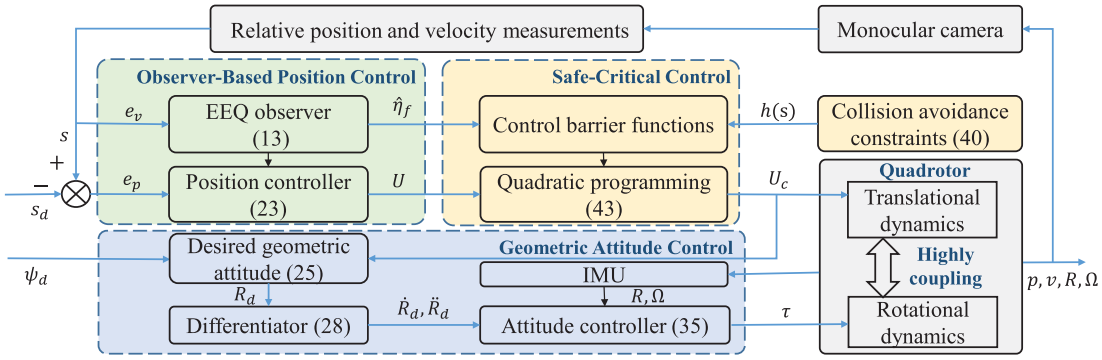

Fig. 2. Structure of the safety-critical visual servoing control scheme.

while guaranteeing the relative altitude is larger than the smallest collision avoidance radii as $\boldsymbol{e}_3^T \boldsymbol{s} \geq \gamma$.

III. Control Design

The main elements of the proposed safety control system are shown in Fig. 2, which contains a high-level PBVS controller and a low-level safety-critical controller.

1) The high-level controller is proposed to reject the external uncertainties with input saturation.
2) The low-level controller is designed to avoid collision during the tracking process. By this means, the collisions between the quadrotor and the mobile base can be avoided, while the adverse effect of external disturbances and unknown linear acceleration of the targets can be compensated, which improves the autonomy and safety of the quadrotor in the real world.

A. Estimation Error Quantified (EEQ) Observer

An EEQ observer is designed to identify and compensate for the translational disturbance $\boldsymbol{\eta}_f$, as well as guaranteeing the estimated error with a nonnegative upper bound M_b such that

$$\|\hat{\boldsymbol{\eta}}_f - \boldsymbol{\eta}_f\| \leq M_b \quad \forall t \geq 0. \tag{12}$$

For the translational motion subsystem (10), an EEQ observer is designed as

$$\begin{cases} \hat{\boldsymbol{\eta}}_f = \boldsymbol{z} + \alpha \boldsymbol{e}_v \\ \dot{\boldsymbol{z}} = -\alpha(\boldsymbol{U} + g\boldsymbol{e}_3 + \boldsymbol{z} + \alpha \boldsymbol{e}_v) \end{cases} \tag{13}$$

where $\alpha > 0$ is the observer gain to be tuned, and $\boldsymbol{z}$ is an auxiliary variable. Define the estimated error as

$$\boldsymbol{e}_\eta = \hat{\boldsymbol{\eta}}_f - \boldsymbol{\eta}_f. \tag{14}$$

Then the error dynamics is given by

$$\begin{aligned} \dot{\boldsymbol{e}}_\eta &= \dot{\boldsymbol{z}} + \alpha \dot{\boldsymbol{e}}_v - \dot{\boldsymbol{\eta}}_f \\ &= \alpha\left(\dot{\boldsymbol{e}}_v - \boldsymbol{U} - g\boldsymbol{e}_3 - \hat{\eta}_f\right) - \dot{\boldsymbol{\eta}}_f \\ &= -\alpha \boldsymbol{e}_\eta - \dot{\boldsymbol{\eta}}_f. \end{aligned} \tag{15}$$

Choose a Lyapunov candidate function as

$$V_\eta = \boldsymbol{e}_\eta^T \boldsymbol{e}_\eta. \tag{16}$$

Substituting (15) into (16) yields

$$\begin{aligned} \dot{V}_\eta &= 2\boldsymbol{e}_\eta^T \dot{\boldsymbol{e}}_\eta = -2\alpha \|\boldsymbol{e}_\eta\|^2 - 2\boldsymbol{e}_\eta^T \dot{\boldsymbol{\eta}}_f \\ &\leq -2\alpha \|\boldsymbol{e}_\eta\|^2 + 2\bar{\eta}_{f2} \|\boldsymbol{e}_\eta\|. \end{aligned} \tag{17}$$

Using Young's inequality, one has

$$2\bar{\eta}_{f2} \|\boldsymbol{e}_\eta\| \leq \alpha \|\boldsymbol{e}_\eta\|^2 + \frac{\bar{\eta}_{f2}^2}{\alpha}. \tag{18}$$

Then (17) can be rewritten as

$$\dot{V}_\eta \leq -\alpha \|\boldsymbol{e}_\eta\|^2 + \bar{\eta}_{f2}^2 / \alpha^2. \tag{19}$$

Integration of (19) yields the following inequality:

$$\|\boldsymbol{e}_\eta\| \leq \sqrt{\left(\|\boldsymbol{e}_\eta(0)\|^2 - \bar{\boldsymbol{\eta}}_{f2}^2/\alpha^2\right)e^{-\alpha t} + \bar{\eta}_{f2}^2/\alpha^2} \triangleq M_b. \tag{20}$$

Therefore, the transient bound implies that the upper bound on the estimation error for any $t > 0$ can be made arbitrarily small by increasing the design parameter α.

Remark 2: The EEQ observer, proposed in [30], is a generalization of the traditional asymptotic observer that requires the state estimation error to converge to zero. Its essence is to guarantee a quantified boundness of the estimated error, which is important to the low-level safety-critical controller design since CBF constraints rely on the boundedness of the estimation error. The EEQ observer subsumes many types of common observers, such as interval observers, exponentially stable observers, and neural-network-based observers. The exponentially stable observer requires that the equilibrium point is exponentially stable, so it ensures that the estimated error decays exponentially from a maximum initial error bound. Compared to the other two observers, it converges quickly and has the potential to be applied to real-time systems.

B. Observer-Based PBVS Controller With Input Saturation

In this section, we propose an EEQ observer-based controller for the translational subsystem in the presence of unknown external uncertainties and input saturation.

The controller design procedure starts with the following definition of the tracking error signal:

$$\boldsymbol{e}_p = \boldsymbol{s} - \boldsymbol{s}_d. \tag{21}$$

Since $\dot{\boldsymbol{s}}_d = 0$, the translational system model is derived as

$$\begin{cases} \dot{\boldsymbol{e}}_p = \boldsymbol{e}_v \\ \dot{\boldsymbol{e}}_v = \boldsymbol{U} + g\boldsymbol{e}_3 + \boldsymbol{\eta}_f \end{cases}. \tag{22}$$

To achieve the stability of the translational system with external uncertainties and control input saturation. Exploiting the EEQ observer (13), the intermediary translational control law can be designed as

$$\boldsymbol{U} = -b_1 \tanh\left(k_p \boldsymbol{e}_p + k_v \boldsymbol{e}_v\right) - b_2 \tanh(k_v \boldsymbol{e}_v) - \hat{\boldsymbol{\eta}}_f - g\boldsymbol{e}_3 \tag{23}$$

where b_1, b_2, k_p, and k_v are positive constants.

For practical quadrotor dynamic systems, physical input saturation on hardware severely limits system performance. To this end, the restricted intermediary translational control law is proposed and satisfies $\|\boldsymbol{U}\| \leq b_1 + b_2 + \bar{\eta}_{f1} + M_b + g$.

Based on signal $\boldsymbol{U}$, we consider the following thrust force input for the quadrotor:

$$f = -m\boldsymbol{U}^T(\boldsymbol{R}\boldsymbol{e}_3). \tag{24}$$

Remark 3: The EEQ observer-based PBVS controller can compensate for the uncertain landing system dynamics within an exponential error bound, such that the safe control performance and the system robustness can be significantly improved. However, there are currently no constraints on the relative altitude between the quadrotor and the 3-D ground target, making it possible for the quadrotor to collide with the target and cause tracking failure. This problem will be solved by introducing a CBF in the subsequent section.

C. Desired Geometric Attitude Extractions

The designed controller satisfies $\boldsymbol{U} \neq 0$. Then, the desired attitude of the inner loop $\boldsymbol{R}_d = [\boldsymbol{r}_{1,d}, \boldsymbol{r}_{2,d}, \boldsymbol{r}_{3,d}]$ can be calculated as

$$\begin{cases} \boldsymbol{r}_{1,d} = \boldsymbol{r}_{2,d} \times \boldsymbol{r}_{3,d} \\ \boldsymbol{r}_{2,d} = \dfrac{\boldsymbol{r}_{3,d} \times \boldsymbol{\Psi}}{\|\boldsymbol{r}_{3,d} \times \boldsymbol{\Psi}\|} \\ \boldsymbol{r}_{3,d} = -\dfrac{\boldsymbol{U}}{\|\boldsymbol{U}\|} \end{cases} \tag{25}$$

with the desired direction of the first body-fixed axis $\boldsymbol{\Psi} = [\cos\psi_d, \sin\psi_d, 0]^T$, where ψ_d is the desired yaw angle of the quadrotor, and $\boldsymbol{\Psi}$ is not parallel to $\boldsymbol{r}_{3id}$. The corresponding desired angular velocity and its derivative are derived as

$$\boldsymbol{\Omega}_d^{\wedge} = \boldsymbol{R}_d^T \dot{\boldsymbol{R}}_d \tag{26}$$

$$\dot{\boldsymbol{\Omega}}_d^{\wedge} = \left(\boldsymbol{\Omega}_d^{\wedge}\right)^T \boldsymbol{R}_d^T \dot{\boldsymbol{R}}_d + \boldsymbol{R}_d^T \ddot{\boldsymbol{R}}_d. \tag{27}$$

For the sake of avoiding the computational complexity, a high-order sliding mode (HOSM) differentiator is employed to acquire $\dot{\boldsymbol{R}}_d$ and $\ddot{\boldsymbol{R}}_d$. Let $\hat{\boldsymbol{R}}_d$ be the estimated value of $\boldsymbol{R}_d$, and $\widetilde{\boldsymbol{R}} = \boldsymbol{R}_d - \hat{\boldsymbol{R}}_d$. The differentiator requires only information of the output $\boldsymbol{R}_d$ and provides finite-time convergence to the origin for $\widetilde{\boldsymbol{R}}$. The dynamics of the differentiator is

$$\begin{aligned} \dot{\boldsymbol{x}}_1 &= k_{x,1}\|\widetilde{\boldsymbol{R}}\|^{\frac{1}{3}} \operatorname{sign}\left(\widetilde{\boldsymbol{R}}\right) + \boldsymbol{x}_2 \\ \dot{\boldsymbol{x}}_2 &= k_{x,2}\|\widetilde{\boldsymbol{R}}\|^{\frac{2}{3}} \operatorname{sign}\left(\widetilde{\boldsymbol{R}}\right) + \boldsymbol{x}_3 \\ \dot{\boldsymbol{x}}_3 &= k_{x,3} \operatorname{sign}\left(\widetilde{\boldsymbol{R}}\right) \end{aligned} \tag{28}$$

where positive constant gains are selected as $k_{x,1} > 0$, $k_{x,2} > 0$, and $k_{x,3} > 0$. The estimated values are given by $\hat{\boldsymbol{R}}_d = \boldsymbol{x}_1$, $\dot{\hat{\boldsymbol{R}}}_d = \boldsymbol{x}_2$, and $\ddot{\hat{\boldsymbol{R}}}_d = \boldsymbol{x}_3$. The dynamics system (28) is exponentially stable that is already proved in [38], so we can conclude that $\dot{\hat{\boldsymbol{R}}}_d$ and $\ddot{\hat{\boldsymbol{R}}}_d$ will converge to $\dot{\boldsymbol{R}}_d$ and $\ddot{\boldsymbol{R}}_d$.

D. Robust Geometric Attitude Controller on $\mathfrak{so}(3)$

Once $\boldsymbol{R}_d$, $\boldsymbol{\Omega}_d$, and $\dot{\boldsymbol{\Omega}}_d$ are well defined, the inner-loop control torque τ can be designed to track the desired geometric attitude command $\boldsymbol{R}_d$ such that $\boldsymbol{R}^T\boldsymbol{R}_d \to \boldsymbol{I}_3$. In particular, a continuous RISE control structure is used to compensate for attitude disturbances. Denote $\boldsymbol{R}_e = \boldsymbol{R}^T\boldsymbol{R}_d$, then the logarithmic configuration attitude error function on $\mathfrak{so}(3)$ is defined by

$$\boldsymbol{e}_R = \operatorname{Log}(\boldsymbol{R}_e)^{\vee}. \tag{29}$$

Additionally, we can express the angular velocity error as

$$\boldsymbol{e}_{\Omega} = \boldsymbol{R}_e\boldsymbol{\Omega}_d - \boldsymbol{\Omega}. \tag{30}$$

Based on the definition of the principle matrix logarithm (1), the time derivatives of $\boldsymbol{e}_R$ and $\boldsymbol{e}_{\Omega}$ are given by

$$\dot{\boldsymbol{e}}_R = \boldsymbol{C}(\boldsymbol{e}_R)\boldsymbol{e}_{\Omega} \tag{31}$$

$$\boldsymbol{J}\dot{\boldsymbol{e}}_{\Omega} = \boldsymbol{J}\boldsymbol{D} - (\boldsymbol{\tau} - \boldsymbol{\Omega} \times \boldsymbol{J}\boldsymbol{\Omega} + \boldsymbol{d}_{\tau}) \tag{32}$$

where $\boldsymbol{C}(\boldsymbol{e}_R)$ and $\boldsymbol{D}$ are given by

$$\begin{aligned} \boldsymbol{C}(\boldsymbol{e}_R) &= \boldsymbol{I}_3 + \frac{1}{2}\boldsymbol{e}_R^{\wedge} \\ &\quad + \left(1 - \frac{\|\boldsymbol{e}_R\|_2}{2}\cot\left(\frac{\|\boldsymbol{e}_R\|_2}{2}\right)\right)\frac{\left(\boldsymbol{e}_R^{\wedge}\right)^2}{\|\boldsymbol{e}_R\|_2^2} \\ \boldsymbol{D} &= -\boldsymbol{\Omega}^{\wedge}\boldsymbol{R}_e\boldsymbol{\Omega}_d + \boldsymbol{R}_e\dot{\boldsymbol{\Omega}}_d. \end{aligned}$$

Instrumental in our approach, an auxiliary error signal $\boldsymbol{r}$ is introduced to acquire additional design freedom. Denote $\bar{\boldsymbol{e}}_{\Omega} = \boldsymbol{e}_{\Omega} + k_{r,1}\boldsymbol{e}_R$, and

$$\boldsymbol{r} = \dot{\bar{\boldsymbol{e}}}_{\Omega} + k_{r,2}\bar{\boldsymbol{e}}_{\Omega} \tag{33}$$

where $k_{r,1} > 0$ and $k_{r,2} > 0$ are positive constants. It should be pointed out that $\boldsymbol{r}$ will be vital for the next stability proof of RISE even though it does not appear in the control design.

Substituting (31) and (32) into (33), one gets

$$\begin{aligned} \boldsymbol{r} &= \boldsymbol{D} - \boldsymbol{J}^{-1}(\boldsymbol{\tau} - \boldsymbol{\Omega} \times \boldsymbol{J}\boldsymbol{\Omega} + \boldsymbol{d}_{\tau}) \\ &\quad + k_{r,1}\boldsymbol{C}(\boldsymbol{e}_R)\boldsymbol{e}_{\Omega} + k_{r,2}\bar{\boldsymbol{e}}_{\Omega}. \end{aligned} \tag{34}$$

Now a geometric attitude controller is designed as

$$\begin{aligned} \boldsymbol{\tau} &= \left(k_{r,3} + k_{r,2}\right)\bar{\boldsymbol{e}}_{\Omega} + \boldsymbol{\Omega} \times \boldsymbol{J}\boldsymbol{\Omega} \\ &\quad + \boldsymbol{J}\left(\boldsymbol{D} + k_{r,1}\boldsymbol{C}(\boldsymbol{e}_R)\boldsymbol{e}_{\Omega}\right) + \boldsymbol{V}_T \end{aligned} \tag{35}$$

where $\boldsymbol{V}_T \in \mathbb{R}^3$ is the Filippov solution to the following differential equation:

$$\dot{\boldsymbol{V}}_T = k_{r,3}k_{r,2}\bar{\boldsymbol{e}}_{\Omega} - \beta \operatorname{sign}\left(\bar{\boldsymbol{e}}_{\Omega}\right) \tag{36}$$

where $k_{r,3} > 0$ is a positive constant. The geometric attitude controller can avoid the singularities of Euler angles and the ambiguity of quaternions. What is more, a salient highlight

of the designed control law is that asymptotic stability can be achieved for uncertain nonlinear systems.

Condition 1: To achieve the attitude tracking in finite time, the controller gains are suitably selected such that

$$\beta \geq \bar{d}_{\tau 1} + \frac{1}{k_{r,1}} \bar{d}_{\tau 2}. \tag{37}$$

Remark 4: The level of the quadrotor's maneuverability is closely related to the attitude representation methods. Traditional attitude representation methods such as Euler angles and quaternions greatly limit the performance of the flight control algorithm. In contrast, geometric attitude controllers have been developed to use rotation matrices directly to achieve a singularity-free global attitude representation. After rapid development in recent years, the representation of geometric attitude can be summarized as the following two types: real-valued functions and Lie algebra-valued functions. The magnitude of real-valued functions can be depicted by a sine function, resulting in their convergence rate decreasing severely when the axis angle approaches π. However, the magnitude of Lie algebra-valued functions is proportional to the rotation angle. Attitude error configuration on the Lie algebra has advantages in improving tracking performance due to its fast convergence and large-angle maneuverability.

E. Stability Analysis

Before presenting the main result of this section, we state the following lemma which will be invoked later.

Lemma 2 [35]: Let the auxiliary function L be defined as the Filippov solution to the following differential equations:

$$\dot{\boldsymbol{L}}(t) = \boldsymbol{r}^T \left(\dot{\boldsymbol{d}}_\tau - \beta \text{sign}\left(\bar{\boldsymbol{e}}_\Omega \right) \right). \tag{38}$$

If the control gain β is chosen to satisfy sufficient Condition 1, then the function Q defined in the following is positive all the time.

$$\boldsymbol{Q}(t) = \beta \|\bar{\boldsymbol{e}}_\Omega(0)\| - \bar{\boldsymbol{e}}_\Omega(t_0)^T \boldsymbol{d}_\tau(t_0) + \boldsymbol{L}. \tag{39}$$

We now state the stability result for the proposed controller.

Theorem 1: Considering the cascaded system (4) under Assumptions 1 and 2, with the designed thrust force (24) and torque inputs (35), then the whole closed-loop system is uniformly ultimately bounded.

Proof: See the Appendix. □

F. Safety-Critical Controller With Collision Avoidance

To achieve collision avoidance during landing, the relative altitude between a quadrotor and a target should be imposed in the following forward invariant set:

$$\mathcal{L} = \left\{ \boldsymbol{s} \in \mathbb{R}^3 | h(\boldsymbol{s}) \geq 0 \right\} \tag{40}$$

where $h(\boldsymbol{s}) = \|\boldsymbol{e}_3^T \boldsymbol{s}\|^2 - \gamma^2$.

CBFs are a useful tool for rendering the collision-free constraints (40) as forward invariant throughout its state space. Define a zeroing barrier function as

$$H(\boldsymbol{s}) = \dot{h}(\boldsymbol{s}) + k_1 h(\boldsymbol{s}). \tag{41}$$

According to Lemma 1, if the constraint $\dot{H}(\boldsymbol{s}) \geq -k_2 H(\boldsymbol{s})$ is satisfied, then the set (40) is forward invariant. In other words

$$\ddot{h}(\boldsymbol{s}) + (k_1 + k_2)\dot{h}(\boldsymbol{s}) + k_1 k_2 h(\boldsymbol{s}) \geq 0 \tag{42}$$

should be guaranteed, where k_1 and k_2 are positive constants. Using (10), the derivative and the second-order derivative of $h(\boldsymbol{s})$ are given by

$$\dot{h}(\boldsymbol{s}) = 2\left(\boldsymbol{e}_3^T \boldsymbol{s}\right)\left(\boldsymbol{e}_3^T \boldsymbol{e}_v\right)$$
$$\ddot{h}(\boldsymbol{s}) = 2\left(\boldsymbol{e}_3^T \boldsymbol{e}_v\right)\left(\boldsymbol{e}_3^T \boldsymbol{e}_v\right) + 2\left(\boldsymbol{e}_3^T \boldsymbol{s}\right)\boldsymbol{e}_3^T \left(\boldsymbol{U} + g\boldsymbol{e}_3 + \hat{\boldsymbol{\eta}}_f - \boldsymbol{e}_\eta\right).$$

Formulating the control problem as a quadratic program enables us to incorporate constraints into the optimization. Quadratic programming (QP) is employed to minimally adjust the PBVS nominal controller $\boldsymbol{U}$. Using (20), one gets

$$\begin{aligned} \boldsymbol{U}_c^* = \min_{U} \quad & \|\boldsymbol{U}_c - \boldsymbol{U}\|^2 \\ \text{s.t.} \quad & \boldsymbol{A}\boldsymbol{U}_c \leq \boldsymbol{B} \end{aligned} \tag{43}$$

where

$$\boldsymbol{A} = -2\left(\boldsymbol{e}_3^T s\right)\boldsymbol{e}_3^T$$
$$\boldsymbol{B} = (k_1 k_2 - 1)\|\boldsymbol{e}_3^T \boldsymbol{s}\|^2 + 2\left(\boldsymbol{e}_3^T \boldsymbol{e}_v\right)\left(\boldsymbol{e}_3^T \boldsymbol{e}_v\right) - M_b^2 - k_1 k_2 \gamma^2 + 2(k1 + k2)\left(\boldsymbol{e}_3^T \boldsymbol{s}\right)\left(\boldsymbol{e}_3^T \boldsymbol{e}_v\right) + 2\left(\boldsymbol{e}_3^T \boldsymbol{s}\right)\boldsymbol{e}_3^T \left(g\boldsymbol{e}_3 + \hat{\boldsymbol{\eta}}_f\right).$$

Remark 5: The safety-critical control design problem of the quadrotor is addressed by transforming the dynamics (4) into a slow outer loop (7) and a fast inner loop (11) coupled with a nonlinear interconnection term. In practice, the inner loop with fast dynamics can track an attitude command quickly and generate the required torques. The outer loop, as a slow time scale subsystem, allows for real-time tracking and collision avoidance. The low-level safety-critical control scheme focuses on collision constraints imposed to ensure the safe operation of the landing system. In particular, the EEQ observer-based CBF does not rely on a prior bound of the disturbance estimation error since the EEQ observer can guarantee a quantified upper bound on the estimated error.

Remark 6: The CBF is a mathematical tool used to describe constraints and safety boundaries on the state of a system. This cost function can encompass parameters such as vehicle velocity, acceleration, intervehicle distances, and so on while considering both safety constraints and performance requirements. The augmentation of optimization parameters introduces additional dimensions to ensure system safety. However, a substantial optimization scale may impose computational performance burdens. Therefore, in practical applications, it is essential to strike a balance between safety and computational performance to determine the number of constraint conditions. In this study, the proposed CBF constraints are simple because only the altitude constraints between a quadrotor and a 3-D ground target are employed. Consequently, the low-complexity CBF-QP algorithm can be effectively applied to low-cost real quadrotors running at a frequency of about 100 Hz.

IV. Simulations and Experiments

To prove the efficiency of the proposed trajectory tracking scheme, several simulations and experiments were conducted.

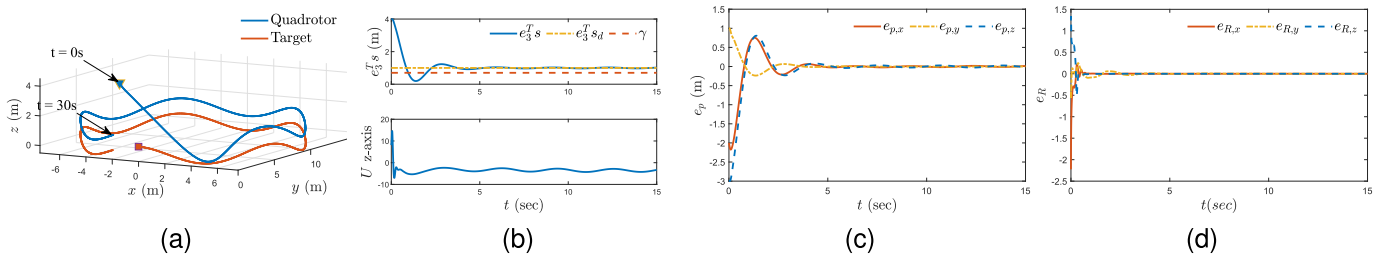

Fig. 3. Simulation A: PBVS controller without collision avoidance. (a) Three-dimensional trajectories of a quadrotor and a target. (b) Time response of relative position and the intermediary translational control law $\boldsymbol{U}$ on the z-axis, where the yellow dotted line represents the desired relative altitude, and the red dashed line indicates the smallest collision avoidance radii. (c) Time response of the position errors. (d) Time response of the attitude errors.

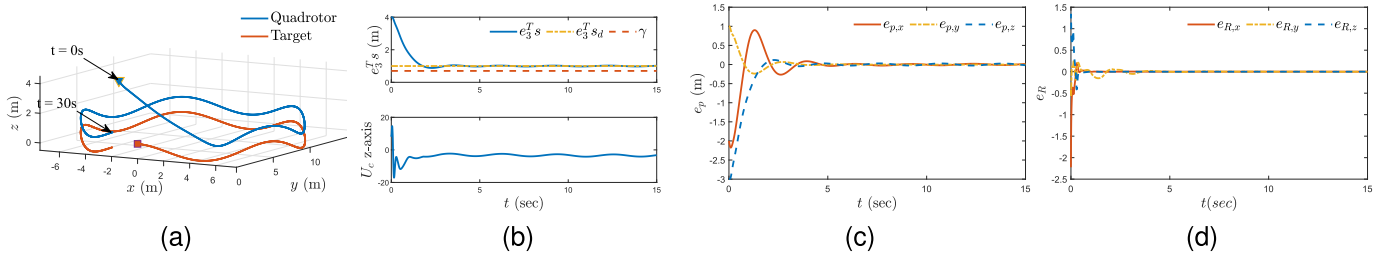

Fig. 4. Simulation B: PBVS controller with collision avoidance. (a) Three-dimensional trajectories of a quadrotor and a target. (b) Time response of relative altitude and the control law $\boldsymbol{U}_c$ on the z-axis. (c) Time response of the position errors. (d) Time response of the attitude errors.

TABLE I
PARAMETERS OF QUADROTORS TRACKING CONTROL

Parameters	Value	Parameters	Value
α	10	b_1	10
b_2	10	k_p	3
k_v	5	$k_{x,1}$	10
$k_{x,2}$	20	$k_{x,3}$	30
$k_{r,1}$	40	$k_{r,2}$	10
$k_{r,3}$	5	β	1
k_1	5	k_2	5

By default, the values of variables are in SI units. The physical properties of the quadrotor are given by: $m = 1.5$ kg, $g = 9.81\text{m/s}^2$, and $\boldsymbol{J} = \text{diag}\{0.0756, 0.0756, 0.1277\}$ kg·m^2/rad^2. The quadrotor has physical dimensions of $0.5 \times 0.5 \times 0.4$ m and is configured with four thrusters. The focal length of an onboard downward camera is 1.8 mm and its resolution is 640×480 pixels. The smallest collision avoidance radii γ is set as 0.7 m. No prior knowledge of the moving target is provided. The quadrotor is expected to stay right above the target at $\boldsymbol{s}_d = [0, 0, 1]^T$. For the repeatability results for both simulation and experiment, the parameters for the landing controllers (29) and (42) are given in Table I.

A. Simulations Result Without Collision Avoidance

Considering a moving target with complex 3-D motions as $\boldsymbol{v}_t = [3\cos(0.4t), 3\sin(0.4t), \sin(2t)]^T$. The wind disturbances $\boldsymbol{d}_f = 0.5[\cos(t), \cos(t), \sin(t)]^T$ and $\boldsymbol{d}_\tau = 1.0[\cos(t), \cos(t), \sin(t)]^T$ are imposed to the quadrotor. The specified velocity profile aims to validate the capability of the proposed controller to effectively handle prospective real-world applications, such as tracking floating vessels or maneuvering vehicles on uneven terrains. The simulation results are shown in Fig. 3. Fig. 3(a) illustrates the 3-D trajectories of a quadrotor and a moving target. Fig. 3(b) depicts the time response of relative position and the intermediary translational control law $\boldsymbol{U}$ on the z-axis, where the yellow dotted line represents the desired relative altitude and the red dashed line indicates the smallest collision avoidance radii. The time responses of position errors and attitude errors of the quadrotor are shown in Fig. 3(c) and (d). Although frequent variations of target velocities arise from certain tracking errors and unknown disturbances, they impose adverse influences on the stability of the quadrotor. It can be seen that the observer can obtain an effective estimate of the external uncertainty from the measurable variables, thus ensuring the tracking performance of the target in the wind disturbance environment. However, the collision avoidance constraint is violated in this case, making it possible for the quadrotor to collide with the target, resulting in tracking failure. This issue will be addressed in the next simulation.

B. Simulations Result With Collision Avoidance

Under the same simulation conditions as Section IV-A, the collision avoidance constraint is taken into consideration. The control command is replaced by the constrained control input (43). The simulation results are shown in Fig. 4. The 3-D trajectories are illustrated in Fig. 4(a). Fig. 4(b) depicts the time response of relative position and the intermediary translational control law $\boldsymbol{U}_c$ on the z-axis. The time responses of position errors and attitude errors of the quadrotor are shown in Fig. 4(c) and (d). It can be seen that the position error converges softly, resulting in a smooth quadrotor tracking trajectory. During the tracking process, the quadrotor does not violate the designed safety-critical constraints, ensuring collision avoidance performance. Therefore, the studies show the superior robustness of the proposed method in handling both external uncertainties and collision avoidance.

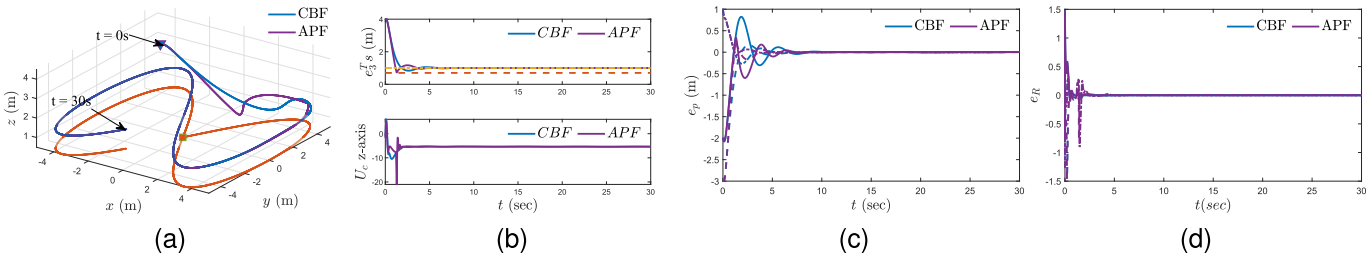

Fig. 5. Comparative study for the collision avoidance performance of the proposed CBF-based controller and the APF-based controller. (a) Trajectories of a quadrotor and a moving target, where the purple solid line represents the APF-based controller, the blue solid line is the proposed controller, and the red solid line is the target's trajectory. (b) Time response of relative altitude and the control law $\boldsymbol{U}_c$ on the z-axis. (c) Time response of the position errors. (d) Time response of the attitude errors.

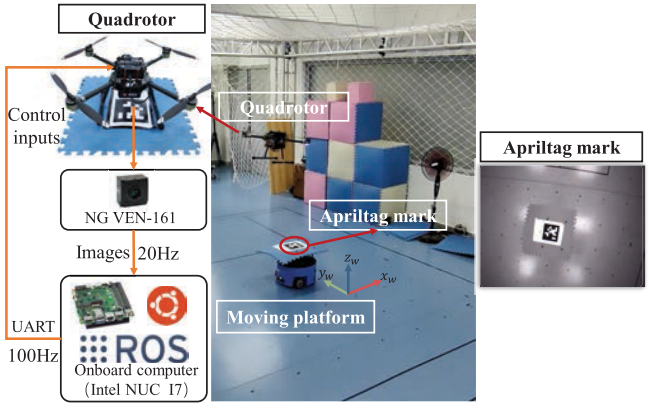

Fig. 6. Experimental system and the internal view from the onboard camera.

C. Comparative Studies for Collision Avoidance Performance

To analyze the collision avoidance performance of the proposed controller, we evaluated the CBF-based controller defined in (43) and compared the results with those of the approach based on the APF in [18]. The target is endowed with complex motions involving acceleration and deceleration, and an "8"-shaped reference trajectory is chosen as $\boldsymbol{v}_t = [\cos(0.2t), 2\cos(0.4t), 0]^T$. The results are shown in Fig. 5. Fig. 5(a) illustrates the 3-D trajectories of a quadrotor and a moving target, where the purple solid line represents the APF-based controller and the blue solid line represents the proposed controller. Fig. 5(b) depicts the time response of relative position and the intermediary translational control law $\boldsymbol{U}_c$ on the z-axis. The time responses of position errors and attitude errors of the quadrotor are shown in Fig. 5(c) and (d). It can be seen that although both methods can achieve collision avoidance, the quadrotor's trajectory using the APF method is more aggressive and brings potential collision danger in the real landing mission. On the contrary, the trajectory of the CBF method is smoother and more suitable in practice. Therefore, the CBF method is superior to the APF method in providing smooth landing behavior while avoiding collision at a lower energy cost.

D. Experimental Results

In addition to a comprehensive simulation study, we further implement the proposed control scheme in a real-world experiment on the quadrotor developed in our Robotic Laboratory. We refer readers to the accompanying video at https://youtu.be/6zv-eq0BxZc for a better demonstration of the three flights. As shown in Fig. 6, the entire experimental platform includes a quadrotor, a down-looking monocular camera, and a mobile robot attached to an AprilTag mark. An electric fan is utilized to simulate a windy environment with an average wind speed of 0.312 m/s. The airflow generated by the fan is directed along the negative x-axis. The Daheng NG VEN-161 is used to get its gray image at 20 Hz. The quadrotor detects the target visual mark by the AprilTag2 algorithm [33]. The image-processing algorithm and the landing control law are implemented directly on an Intel NUC i7 PC onboard the quadrotor. The feedback control loop runs at a frequency of about 100 Hz. The proposed algorithm is implemented in the robot operating system (ROS) Neotic, running on Ubuntu 20.04. Three experiment cases are shown to illustrate the performance of the proposed controller.

Case 1: Tracking a stationary target.
Case 2: Tracking a dynamic target with linear motion.
Case 3: Tracking a dynamic target with complex motion.

In the first case, the quadrotor tracks a stationary target in a windy environment. The experimental results are shown in Fig. 7. Fig. 7(a) illustrates the trajectories of a quadrotor and a moving target recorded by the OptiTrack system. Fig. 7(b) and (c) shows the time responses of the position errors and the attitude errors. Fig. 7(d) depicts the time response of the relative attitude between the quadrotor and target, the torque inputs $\tau = [\tau_x, \tau_y, \tau_z]^T$, and the net thrust force f of the quadrotor. It can be seen that the quadrotor tracks the target effectively and ensures collision avoidance constraints throughout the tracking process. Therefore, the experimental results show the effectiveness of the proposed method for disturbance rejection and collision avoidance.

In the second case, the quadrotor tracks a dynamic target with linear motion. The experimental results are shown in Fig. 8. Fig. 8(a) illustrates the trajectories of a quadrotor and a moving target. Fig. 8(b) and (c) shows the time responses of the position errors and the attitude errors. Fig. 8(d) depicts the time response of the relative altitude, the torque inputs $\tau = [\tau_x, \tau_y, \tau_z]^T$, and net thrust force f. It can observed that the quadrotor can track moving targets without collision in the presence of uncertain targets and external disturbances.

In the third case, the quadrotor was required to track a moving target moving in an "8"-shaped trajectory. The experimental results are shown in Fig. 9. Fig. 9(a) illustrates

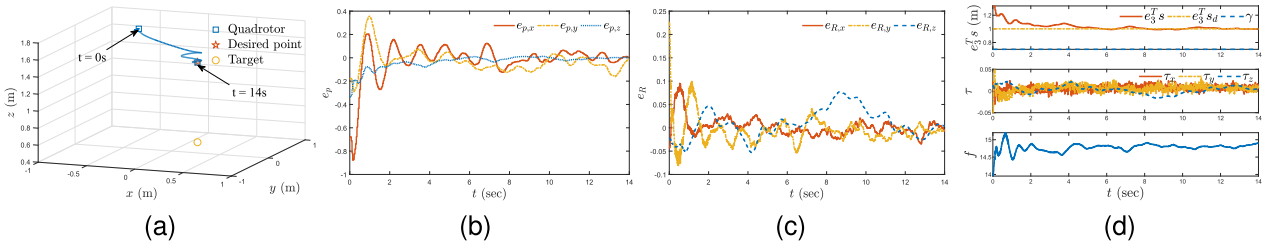

Fig. 7. Experiment 1: Tracking a stationary target. (a) Three-dimensional trajectories of a quadrotor and a target. (b) Time response of the position errors. (c) Time response of the attitude errors. (d) Time response of relative position between the quadrotor and the target on the z-axis, the torque inputs $\tau = [\tau_x, \tau_y, \tau_z]^T$, and net thrust force f of the quadrotor.

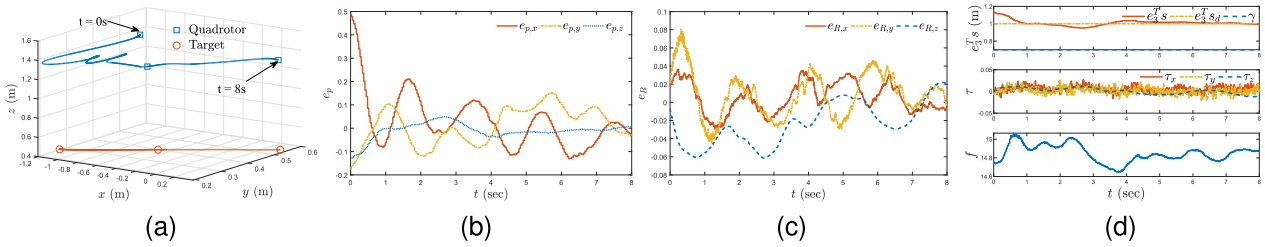

Fig. 8. Experiment 2: Tracking a dynamic target with linear motion. (a) Three-dimensional trajectories of a quadrotor and a target. (b) Time response of the position errors. (c) Time response of the attitude errors. (d) Time response of relative altitude, the torque inputs, and net thrust force.

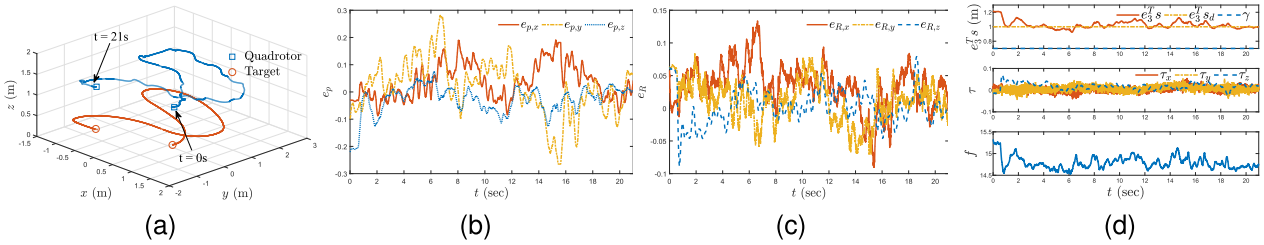

Fig. 9. Experiment 3: Tracking a dynamic target moving in an "8"-shaped trajectory. (a) Three-dimensional trajectories of a quadrotor and a target. (b) Time response of the position errors. (c) Time response of the attitude errors. (d) Time response of relative altitude, the torque inputs, and net thrust.

the trajectories of a quadrotor and a moving target. Fig. 9(b) and (c) shows the time responses of the position errors and the attitude errors. Fig. 9(d) depicts the time response of the relative altitude, the torque inputs $\tau = [\tau_x, \tau_y, \tau_z]^T$, and net thrust force f. Although the external disturbances and the complex motion of the target cause certain tracking errors, the quadrotor tracks the moving target in real-time without violating the collision avoidance constraint. The experimental results show the robustness of the proposed method against uncertain targets with complex motions.

E. Experimental Discussion

The proposed framework encompasses active position estimation and conflict-free landing control. AprilTag, as a visual reference system, allows for fast localization, with real-time performance achievable even on cell-phone grade processors. In practice, cameras suffer from nonlinear image distortion, which includes radial distortion caused by the lens shape during light propagation and tangential distortion caused by mechanical mounting. To tackle this issue, distortion coefficients can be obtained through camera calibration. Subsequently, the distortion can be corrected using the classic distortion equation in the camera coordinate system [38], and the transformed, undistorted points can then be accurately mapped to their real coordinates on the pixel plane using the camera's intrinsic matrix. The nominal controllers (24) and (35) have a straightforward form. Furthermore, the CBF offers an effective and minimally intrusive method to handle landing collision constraints. As a result, the solution is of considerably low computational complexity, making it suitable for this type of vehicle with low cost, real-time operation, and limited computation ability. The term "unknown targets" pertains to the absence of explicit communication between the quadrotor and the landing target, as well as the lack of prior knowledge regarding the target's motion model. Since this work primarily focuses on the tracking and landing task of the quadrotor, the consideration of carrying various payloads has not been taken into account. To implement active physical interaction with the environment, we are interested in achieving simultaneous transportation and landing tasks. The fluctuations observed around $t = 13$ in Fig. 7(a) are likely caused by the poor localization quality of the AprilTag. The wavy motion is seen in Fig. 8(a) around $t = 2$ and Fig. 9(a) around $t = 1$ is a result of low operational frequencies due to hardware limitations, which leads to a slow transient response of the quadrotor. Additionally, the pronounced fluctuations around $t = 20$ in Fig. 9(a) are caused by the ground target's executing sharp turns with high curvature. While

transient fluctuations stemming from hardware limitations are inevitable, our plan includes refining the localization algorithm and incorporating considerations for the target's high-curvature motion to enhance the steady-state tracking performance.

The effectiveness and repeatability of the proposed method for both stationary and moving targets have been demonstrated through three sets of experiments. Presently, well-established solutions are available for handling external time-varying disturbances, including but not limited to sliding mode observers and extended state observers. It is noteworthy that the presented safety-critical control scheme not only possesses advantages in disturbance rejection but, more importantly, achieves collision avoidance capability in the presence of disturbances by ensuring quantitative estimation errors. On the other hand, although the electric fan provides a constant wind speed, the disturbance experienced by one side of the quadrotor varies as it approaches and moves away from the fan due to the air resistance generated by the rotors. Disturbance is more pronounced when in proximity to the electric fan and diminishes when distanced from it. Consequently, the experimental results not only showcase the effectiveness of the proposed algorithm in suppressing external disturbances but also emphasize its feasibility and performance in collision avoidance for targets in different motion states.

V. Conclusion

In this article, a safety-critical landing control scheme for quadrotors with disturbances rejection and collision avoidance is proposed. An EEQ observer was designed to estimate the translational uncertainties. Then, an EEQ observer-based CBF-QP was formulated to achieve the collision avoidance of an uncertain quadrotor system. Moreover, a geometric attitude controller was developed with a continuous RISE control structure. It was able to compensate for unknown attitude disturbances and achieve asymptotic attitude tracking. The stability of the closed-loop cascaded system was proved using the Lyapunov stability theory. Simulations and experimental results have demonstrated the effectiveness and superior performance of the proposed controller in handling external disturbances and collisions between vehicles.

Appendix
Proof of Theorem 1

In what follows, we proceed in three steps to prove the stability of the control system.

Step 1: Stability of the attitude error dynamics.

Substituting (35) into (34), then the auxiliary attitude error dynamics are given by

$$\boldsymbol{J}\dot{\boldsymbol{r}} = -k_{r,3}\boldsymbol{r} + \beta \text{sign}\left(\bar{\boldsymbol{e}}_\Omega\right) - \dot{\boldsymbol{d}}_\tau. \tag{44}$$

Consider the following Lyapunov candidate function:

$$V_1 = \frac{1}{2}c_1\boldsymbol{e}_R^T\boldsymbol{e}_R + \frac{1}{2}\bar{\boldsymbol{e}}_\Omega^T\bar{\boldsymbol{e}}_\Omega + \frac{1}{2}\boldsymbol{r}^T\boldsymbol{J}\boldsymbol{r} + \boldsymbol{Q} \tag{45}$$

where c_1 is a positive constant. Using (1) and (33), the time derivative of V_1 is given by

$$\begin{aligned}\dot{V}_1 = {} & \frac{c_1}{2}\text{tr}\left(\left(\text{Log}(R_e)\right)^T\boldsymbol{e}_R\right) + \bar{\boldsymbol{e}}_\Omega^T\left(\boldsymbol{r} - k_{r,2}\bar{\boldsymbol{e}}_\Omega\right) \\ & + -k_{r,3}\boldsymbol{r}^T\boldsymbol{r} - \boldsymbol{r}^T\left(\dot{\boldsymbol{d}}_\tau - \beta_2\text{sign}\left(\bar{\boldsymbol{e}}_\Omega\right)\right) + \dot{\boldsymbol{Q}} \\ = {} & c_1\boldsymbol{e}_R^T\boldsymbol{e}_\Omega - k_{r,2}\bar{\boldsymbol{e}}_\Omega^T\bar{\boldsymbol{e}}_\Omega + \bar{\boldsymbol{e}}_\Omega^T\boldsymbol{r} - k_{r,3}\boldsymbol{r}^T\boldsymbol{r} \\ \le {} & c_1\boldsymbol{e}_R^T\boldsymbol{e}_\Omega - k_{r,2}\|\boldsymbol{e}_\Omega\|^2 - k_{r,2}k_{r,1}^2\|\boldsymbol{e}_R\|^2 \\ & + \bar{\boldsymbol{e}}_\Omega^T r - k_{r,3}\|\boldsymbol{r}\|^2. \end{aligned} \tag{46}$$

Using Young's inequality, one has

$$c_1\boldsymbol{e}_R^T\boldsymbol{e}_\Omega \le \frac{c_1}{2}\|\boldsymbol{e}_R\|^2 + \frac{c_1}{2}\|\boldsymbol{e}_\Omega\|^2 \tag{47}$$

$$\bar{\boldsymbol{e}}_\Omega^T\boldsymbol{r} \le \sigma_1\|\bar{\boldsymbol{e}}_\Omega\|^2 + \frac{1}{4\sigma_1}\|\boldsymbol{r}\|^2 \tag{48}$$

where σ_1 is a positive constant. Based on the triangle inequality $\|\bar{\boldsymbol{e}}_\Omega\|^2 \le \|\boldsymbol{e}_\Omega\|^2 + \|k_{r,1}\boldsymbol{e}_R\|^2$, one gets

$$\bar{\boldsymbol{e}}_\Omega^T\boldsymbol{r} \le \sigma_1\left(\|\boldsymbol{e}_\Omega\|^2 + \|k_{r,1}\boldsymbol{e}_R\|^2\right) + \frac{1}{4\sigma_1}\|\boldsymbol{r}\|^2. \tag{49}$$

Let $\boldsymbol{z} = [\boldsymbol{e}_R, \boldsymbol{e}_\Omega, \boldsymbol{r}]^T$, one has

$$\dot{V}_1 \le -\boldsymbol{z}^T\boldsymbol{W}\boldsymbol{z} \tag{50}$$

where $\boldsymbol{W} = \text{diag}([w_1, w_2, w_3])$ with $w_1 = c_1\lambda_{\min}(k_{r,1}) - (c_1/2)$, $w_2 = \lambda_{\min}(k_{r,2}) - (c_1/2) - \sigma_1$, and $w_3 = \lambda_{\min}(k_{r,3}) - (1/4\sigma_1)$. If we choose appropriate positive c_1, σ_1 and positive definite gain matrices $k_{r,1}$, $k_{r,2}$, and $k_{r,3}$ to satisfy

$$\lambda_{\min}\left(k_{r,1}\right) > \frac{1}{2},\ \lambda_{\min}\left(k_{r,2}\right) > \frac{c_1}{2} + \sigma_1,\ \lambda_{\min}\left(k_{r,3}\right) > \frac{1}{4\sigma_1}$$

such that $w_1 > 0$, $w_2 > 0$, and $w_3 > 0$, and the matrix W_2 is positive definite. Therefore, the equilibrium point of the attitude and angular velocity error is exponentially stable.

Step 2: Stability of the translational error dynamics.

Substituting (23) into (22), then the translational error dynamics is given by

$$\begin{cases} \dot{\boldsymbol{e}}_p = \boldsymbol{e}_v \\ \dot{\boldsymbol{e}}_v = -b_1\tanh\left(k_p\boldsymbol{e}_p + k_v\boldsymbol{e}_v\right) - b_2\tanh(k_v\boldsymbol{e}_v) - \boldsymbol{e}_\eta \end{cases} \tag{51}$$

Taking the Lyapunov candidate function as

$$V_2 = b_1\ln\left(\cosh\left(k_p\boldsymbol{e}_p + k_v\boldsymbol{e}_v\right)\right) + b_2\ln(\cosh(k_v\boldsymbol{e}_v)) \tag{52}$$

$$+ \frac{k_p}{2}\boldsymbol{e}_v^T\boldsymbol{e}_v + V_\eta. \tag{53}$$

The time derivative of V_2 is given by

$$\begin{aligned}\dot{V}_2 = {} & b_1\left(k_p\dot{\boldsymbol{e}}_p + k_v\dot{\boldsymbol{e}}_v\right)^T\tanh\left(k_p\boldsymbol{e}_p + k_v\boldsymbol{e}_v\right) \\ & + b_2k_p\dot{\boldsymbol{e}}_v^T\tanh(k_v\boldsymbol{e}_v) + \boldsymbol{e}_v^T\dot{\boldsymbol{e}}_v + \dot{V}_\eta. \end{aligned} \tag{54}$$

For ease of notation, denote $\boldsymbol{w}_1 = \tanh(k_p\boldsymbol{e}_p + k_v\boldsymbol{e}_v)$ and $\boldsymbol{w}_2 = \tanh(k_v\boldsymbol{e}_v) + (1/b_2)\boldsymbol{e}_\eta$, then $\dot{\boldsymbol{e}}_v = -b_1\boldsymbol{w}_1 - b_2\boldsymbol{w}_2$. Since the boundedness of $\boldsymbol{e}_\eta$ is given by (20), one has

$$\begin{aligned}\|\dot{\boldsymbol{e}}_v\| \le {} & b_1\|\tanh\left(k_p\boldsymbol{e}_p + k_v\boldsymbol{e}_v\right)\| + b_2\|\tanh(k_v\boldsymbol{e}_v) \\ & + \frac{1}{b_2}\boldsymbol{e}_\eta\| \le b_1 + b_2 + M_b. \end{aligned} \tag{55}$$

Thus, $\dot{\boldsymbol{e}}_v$ is bounded. Now, V_2 can be rewritten as

$$\begin{aligned}\dot{V}_2 \le {} & b_1\left(k_p\dot{\boldsymbol{e}}_v + k_v(-b_1\boldsymbol{w}_1 - b_2\boldsymbol{w}_2)\right)^T\boldsymbol{w}_1 \\ & + b_2k_v(-b_1\boldsymbol{w}_1 - b_2\boldsymbol{w}_2)^T\boldsymbol{w}_2 - k_v\boldsymbol{e}_v^T\boldsymbol{e}_\eta \\ & + k_p\boldsymbol{e}_v^T(-b_1\boldsymbol{w}_1 - b_2\boldsymbol{w}_2) + \dot{V}_\eta. \end{aligned} \tag{56}$$

Substituting the inequality (19) into (56), one gets

$$\dot{V}_2 \le -k_v\|b_1\boldsymbol{w}_1 + b_2\boldsymbol{w}_2\|^2 - k_p b_2 \boldsymbol{e}_v^T \tanh(k_v\boldsymbol{e}_v) - k_v\dot{\boldsymbol{e}}_v^T\boldsymbol{e}_\eta - \alpha\|\boldsymbol{e}_\eta\|^2 + k_p b_2 \boldsymbol{e}_v^T\boldsymbol{e}_\eta + \bar{\eta}_f^2/\alpha^2. \quad (57)$$

Using (55), we obtain

$$\dot{V}_2 \le -k_v\|b_1\boldsymbol{w}_1 + b_2\boldsymbol{w}_2\|^2 - k_p b_2 \boldsymbol{e}_v^T \tanh(k_v\boldsymbol{e}_v) - \alpha\|\boldsymbol{e}_\eta\|^2 + k_v(b_1+b_2+M_b)M_b + k_p b_2\|\boldsymbol{e}_v\|M_b + \bar{\eta}_f^2/\alpha^2.$$

Since $\boldsymbol{e}_v^T\tanh(k_v\boldsymbol{e}_v) \ge 0$, $-k_v\|b_1\boldsymbol{w}_1 + b_2\boldsymbol{w}_2\|^2 - k_p b_2\boldsymbol{e}_v^T\tanh(k_v\boldsymbol{e}_v) < 0$ always holds for $\|\boldsymbol{e}_p\| \ne 0$ or $\|\boldsymbol{e}_v\| \ne 0$. So, for any δ, there is some finite time t_δ, when $\|\boldsymbol{e}_p\| \ge \delta$, such that $\dot{V}_2 \le 0$. As a result, $\|\boldsymbol{e}_p\|$ converges to and remains in a tight set of radius δ in finite time t_δ. Therefore, the translational subsystem (10) is uniformly ultimately bounded.

Step 3: Stability of the overall system with the coupling term. Based on [36], for the cascaded system composed of (7) and (11), if the following conditions are satisfied, then the closed-loop system is uniformly ultimately bounded.

1) The outer-loop subsystem (10) is uniformly ultimately bounded.
2) The interloop subsystem (11) is exponentially stable.
3) The coupling term $\boldsymbol{\chi}$ satisfies $\|\boldsymbol{\chi}\| \le c\|\boldsymbol{e}_R\|$, with c as a positive constant.

In Step 1, the rotational error subsystem (11) has been proven to be exponentially stable. The translational error subsystem (10) has also been proven to be uniformly ultimately bounded in Step 2. Next, we will give proof of the third condition about the coupling term $\boldsymbol{\chi}$.

Substituting (24) into (8), we obtain

$$\|\boldsymbol{\chi}\| \le \|\boldsymbol{U}\|\|\left(\boldsymbol{e}_3^T\boldsymbol{R}_d^T\boldsymbol{R}\boldsymbol{e}_3\right)\boldsymbol{R}\boldsymbol{e}_3 - \boldsymbol{R}_d\boldsymbol{e}_3\|. \quad (58)$$

Since $(\boldsymbol{e}_3^T\boldsymbol{R}_d^T\boldsymbol{R}\boldsymbol{e}_3)\boldsymbol{R}\boldsymbol{e}_3 - \boldsymbol{R}_d\boldsymbol{e}_3$ represents the sine of the angle between $\boldsymbol{R}\boldsymbol{e}_3$ and $\boldsymbol{R}_d\boldsymbol{e}_3$, and $\boldsymbol{e}_R$ represents the eigen-axis rotation angle between $\boldsymbol{R}$ and $\boldsymbol{R}_d$, then the last term of (58) is bounded, and

$$\|\left(\boldsymbol{e}_3^T\boldsymbol{R}_d^T\boldsymbol{R}\boldsymbol{e}_3\right)\boldsymbol{R}\boldsymbol{e}_3 - \boldsymbol{R}_d\boldsymbol{e}_3\| \le \|\boldsymbol{e}_R\|. \quad (59)$$

Therefore, the coupling term $\boldsymbol{\chi}$ satisfies

$$\|\boldsymbol{\chi}\| \le c\|\boldsymbol{e}_R\| \quad (60)$$

where $c = \max(\|\boldsymbol{U}\|) = b_1 + b_2 + \bar{\eta}_{f1} + M_b + g$ is a bounded positive constant. Since $\boldsymbol{e}_R$ converges exponentially to 0, the whole closed-loop system is stable. This completes the proof.

REFERENCES

[1] X. Zhang, Y. Chu, Y. Liu, X. Zhang, and Y. Zhuang, "A novel informative autonomous exploration strategy with uniform sampling for quadrotors," *IEEE Trans. Ind. Electron.*, vol. 69, no. 12, pp. 13131–13140, Dec. 2022.

[2] T. Tomic et al., "Toward a fully autonomous UAV: Research platform for indoor and outdoor urban search and rescue," *IEEE Robot. Autom. Mag.*, vol. 19, no. 3, pp. 46–56, Sep. 2012.

[3] A. V. Borkar, S. Hangal, H. Arya, A. Sinha, and L. Vachhani, "Reconfigurable formations of quadrotors on Lissajous curves for surveillance applications," *Eur. J. Control*, vol. 56, pp. 274–288, Nov. 2020.

[4] D. Cabecinhas, R. Naldi, C. Silvestre, R. Cunha, and L. Marconi, "Robust landing and sliding maneuver hybrid controller for a quadrotor vehicle," *IEEE Trans. Control Syst. Technol.*, vol. 24, no. 2, pp. 400–412, Mar. 2016.

[5] X. Liang, Y. Fang, N. Sun, and H. Lin, "Nonlinear hierarchical control for unmanned quadrotor transportation systems," *IEEE Trans. Ind. Electron.*, vol. 65, no. 4, pp. 3395–3405, Apr. 2018.

[6] R. Mebarki, V. Lippiello, and B. Siciliano, "Nonlinear visual control of unmanned aerial vehicles in GPS-denied environments," *IEEE Trans. Robot.*, vol. 31, no. 4, pp. 1004–1017, Aug. 2015.

[7] Z. Cao et al., "Image dynamics-based visual servoing for quadrotors tracking a target with a nonlinear trajectory observer," *IEEE Trans. Syst., Man, Cybern., Syst.*, vol. 50, no. 1, pp. 376–384, Jan. 2020.

[8] P. Serra, R. Cunha, T. Hamel, D. Cabecinhas, and C. Silvestre, "Landing of a quadrotor on a moving target using dynamic image-based visual servo control," *IEEE Trans. Robot.*, vol. 32, no. 6, pp. 1524–1535, Dec. 2016.

[9] Y. Huang, M. Zhu, Z. Zheng, and K. H. Low, "Homography-based visual servoing for underactuated VTOL UAVs tracking a 6-DOF moving ship," *IEEE Trans. Veh. Technol.*, vol. 71, no. 3, pp. 2385–2398, Mar. 2022.

[10] W. Zhao, H. Liu, F. L. Lewis, K. P. Valavanis, and X. Wang, "Robust visual servoing control for ground target tracking of quadrotors," *IEEE Trans. Control Syst. Technol.*, vol. 28, no. 5, pp. 1980–1987, Sep. 2020.

[11] J. Park, Y. Kim, and S. Kim, "Landing site searching and selection algorithm development using vision system and its application to quadrotor," *IEEE Trans. Control Syst. Technol.*, vol. 23, no. 2, pp. 488–503, Mar. 2015.

[12] H. Rios, R. Falcon, O. A. Gonzalez, and A. Dzul, "Continuous sliding-mode control strategies for quadrotor robust tracking: Real-time application," *IEEE Trans. Ind. Electron.*, vol. 66, no. 2, pp. 1264–1272, Feb. 2019.

[13] H. Liu, J. Xi, and Y. Zhong, "Robust attitude stabilization for nonlinear quadrotor systems with uncertainties and delays," *IEEE Trans. Ind. Electron.*, vol. 64, no. 7, pp. 5585–5594, Jul. 2017.

[14] H. Xie and A. F. Lynch, "Input saturated visual servoing for unmanned aerial vehicles," *IEEE/ASME Trans. Mechatronics*, vol. 22, no. 2, pp. 952–960, Apr. 2017.

[15] J. Dentler, S. Kannan, M. A. O. Mendez, and H. Voos, "A real-time model predictive position control with collision avoidance for commercial low-cost quadrotors," in *Proc. IEEE Conf. Control Appl. (CCA)*, Sep. 2016, pp. 519–525.

[16] Y. Wang and S. Boyd, "Fast model predictive control using online optimization," *IEEE Trans. Control Syst. Technol.*, vol. 18, no. 2, pp. 267–278, Mar. 2010.

[17] J. C. Pereira, V. J. S. Leite, and G. V. Raffo, "Nonlinear model predictive control on SE(3) for quadrotor trajectory tracking and obstacle avoidance," in *Proc. 19th Int. Conf. Adv. Robot. (ICAR)*, Dec. 2019, pp. 155–160.

[18] K. Chang, Y. Xia, K. Huang, and D. Ma, "Obstacle avoidance and active disturbance rejection control for a quadrotor," *Neurocomputing*, vol. 190, pp. 60–69, May 2016.

[19] A. D. Ames, X. Xu, J. W. Grizzle, and P. Tabuada, "Control barrier function based quadratic programs for safety critical systems," *IEEE Trans. Autom. Control*, vol. 62, no. 8, pp. 3861–3876, Aug. 2017.

[20] L. Wang, A. D. Ames, and M. Egerstedt, "Safe certificate-based maneuvers for teams of quadrotors using differential flatness," in *Proc. IEEE Int. Conf. Robot. Autom. (ICRA)*, May 2017, pp. 3293–3298.

[21] M. Khan, M. Zafar, and A. Chatterjee, "Barrier functions in cascaded controller: Safe quadrotor control," in *Proc. Amer. Control Conf. (ACC)*, Jul. 2020, pp. 1737–1742.

[22] G. Wu and K. Sreenath, "Safety-critical and constrained geometric control synthesis using control Lyapunov and control barrier functions for systems evolving on manifolds," in *Proc. Amer. Control Conf. (ACC)*, Jul. 2015, pp. 2038–2044.

[23] G. Wu and K. Sreenath, "Safety-critical control of a planar quadrotor," in *Proc. Amer. Control Conf. (ACC)*, 2016, pp. 2252–2258.

[24] M. Khan, T. Ibuki, and A. Chatterjee, "Safety uncertainty in control barrier functions using Gaussian processes," in *Proc. IEEE Int. Conf. Robot. Autom. (ICRA)*, May 2021, pp. 6003–6009.

[25] L. Wang, E. A. Theodorou, and M. Egerstedt, "Safe learning of quadrotor dynamics using barrier certificates," in *Proc. Int. Conf. Robot. Autom. (ICRA)*, May 2018, pp. 2460–2465.

[26] L. Zheng, R. Yang, J. Pan, and H. Cheng, "Safe learning-based tracking control for quadrotors under wind disturbances," in *Proc. Amer. Control Conf. (ACC)*, May 2021, pp. 3638–3643.

[27] M. Jankovic, "Robust control barrier functions for constrained stabilization of nonlinear systems," *Automatica*, vol. 96, pp. 359–367, Oct. 2018.

[28] K. Garg and D. Panagou, "Robust control barrier and control Lyapunov functions with fixed-time convergence guarantees," in *Proc. Amer. Control Conf. (ACC)*, 2021, pp. 2292–2297.
[29] Q. Nguyen and K. Sreenath, "Robust safety-critical control for dynamic robotics," *IEEE Trans. Autom. Control*, vol. 67, no. 3, pp. 1073–1088, Mar. 2022.
[30] Y. Wang and X. Xu, "Observer-based control barrier functions for safety critical systems," in *Proc. Amer. Control Conf. (ACC)*, 2022, pp. 709–714.
[31] X. Xu, P. Tabuada, J. W. Grizzle, and A. D. Ames, "Robustness of control barrier functions for safety critical control," *IFAC-PapersOnLine*, vol. 48, no. 27, pp. 54–61, 2015.
[32] M. Fiala, "Designing highly reliable fiducial markers," *IEEE Trans. Pattern Anal. Mach. Intell.*, vol. 32, no. 7, pp. 1317–1324, Jul. 2010.
[33] J. Wang and E. Olson, "AprilTag 2: Efficient and robust fiducial detection," in *Proc. IEEE/RSJ Int. Conf. Intell. Robots Syst. (IROS)*, Oct. 2016, pp. 4193–4198.
[34] A. Borowczyk, D. T. Nguyen, A. P. V. Nguyen, D. Q. Nguyen, D. Saussie, and J. L. Ny, "Autonomous landing of a multirotor micro air vehicle on a high velocity ground vehicle," *IFAC-PapersOnLine*, vol. 50, pp. 10488–10494, Jul. 2017.
[35] O. S. Patil, A. Isaly, B. Xian, and W. E. Dixon, "Exponential stability with RISE controllers," *IEEE Control Syst. Lett.*, vol. 6, pp. 1592–1597, 2022.
[36] F. Lamnabhi-Lagarrigue, *Advanced Topics in Control Systems Theory: Lecture Notes From FAP 2004* (Lecture Notes in Control and Information Sciences), vol. 311. London, U.K.: Springer, 2004.
[37] M. T. Angulo, J. A. Moreno, and L. Fridman, "Robust exact uniformly convergent arbitrary order differentiator," *Automatica*, vol. 49, no. 8, pp. 2489–2495, 2013.
[38] Z. Zhang, "A flexible new technique for camera calibration," *IEEE Trans. Pattern Anal. Mach. Intell.*, vol. 22, no. 11, pp. 1330–1334, Nov. 2000.

Jie Lin received the B.S. degree in automation from the College of Electrical Engineering and Automation, Fuzhou University, Fujian, China, in 2019. He is currently pursuing the Ph.D. degree in control science and engineering with Hunan University, Changsha, China.

His current research interests include multirobot systems, visual servoing, and nonlinear control.

Zhiqiang Miao (Member, IEEE) received the B.S. and Ph.D. degrees in electrical and information engineering from Hunan University, Changsha, China, in 2010 and 2016, respectively.

From 2014 to 2015, he was a Visiting Scholar with the University of New Mexico, Albuquerque, NM, USA. From 2016 to 2018, he was a Post-Doctoral Fellow with the Department of Mechanical and Automation Engineering, The Chinese University of Hong Kong, Hong Kong, China. Now he is an Associate Professor with the College of Electrical and Information Engineering, Hunan University. His current research interests include multirobot systems, visual navigation, and nonlinear control.

Yaonan Wang received the B.S. degree in computer engineering from East China Science and Technology University (ECSTU), Fuzhou, China, in 1981, and the M.S. and Ph.D. degrees in electrical engineering from Hunan University, Changsha, China, in 1990 and 1994, respectively.

He has been a Professor with Hunan University, since 1995. His current research interests include robotics, intelligent perception and control, and computer vision for industrial applications.

Prof. Wang is an Academician of the Chinese Academy of Engineering.

Hesheng Wang (Senior Member, IEEE) received the B.Eng. degree in electrical engineering from the Harbin Institute of Technology, Harbin, China, in 2002, and the M.Phil. and Ph.D. degrees in automation and computer-aided engineering from The Chinese University of Hong Kong, Hong Kong, China, in 2004 and 2007, respectively.

He was a Post-Doctoral Fellow and a Research Assistant with the Department of Mechanical and Automation Engineering, The Chinese University of Hong Kong, from 2007 to 2009. He is currently a Professor with the Department of Automation, Shanghai Jiao Tong University. His current research interests include visual servoing, service robots, adaptive robot control, and autonomous driving.

Dr. Wang was the General Chair of the IEEE RCAR 2016 and the Program Chair of the IEEE ROBIO 2014 and IEEE/ASME AIM 2019. He is an Associate Editor of Assembly Automation and the International Journal of Humanoid Robotics, and a Technical Editor of IEEE/ASME TRANSACTIONS ON MECHATRONICS. He served as an Associate Editor for IEEE TRANSACTIONS ON ROBOTICS from 2015 to 2019.

Xiangke Wang received the B.S., M.S., and Ph.D. degrees from the National University of Defense Technology, Changsha, China, in 2004, 2006 and 2012, respectively.

Since 2012, he has been with the College of Mechatronic Engineering and Automation, National University of Defense Technology, and currently he is an Associate Professor. He was a Visiting Ph.D. Student at the Research School of Engineering, Australian National University, supported by the China Scholarship Council from September 2009 to September 2011. His current research interests include coordination control of multiple UAVs, nonlinear control, and robot soccer.

Rafael Fierro (Senior Member, IEEE) received the M.Sc. degree in control engineering from the University of Bradford, Bradford, U.K., in 1990, and the Ph.D. degree in electrical engineering from the University of Texas-Arlington, Arlington, TX, USA, in 1997.

He has been a Professor with the Department of Electrical and Computer Engineering, University of New Mexico, Albuquerque, NM, USA, since 2007. Before joining UNM, he held a Post-Doctoral appointment with the General Robotics, Automation, Sensing and Perception (GRASP) Laboratory, University of Pennsylvania, Philadelphia, PA, USA, and a Faculty position with the Department of Electrical and Computer Engineering, Oklahoma State University, Stillwater, OK, USA.

Dr. Fierro was a recipient of the Fulbright Scholarship, the National Science Foundation CAREER Award, and the 2008 International Society of Automation (ISA) Transactions Best Paper Award. He has served on the Editorial Boards for *Journal of Intelligent and Robotic Systems*, *IEEE Control Systems Magazine*, IEEE TRANSACTIONS ON CONTROL OF NETWORK SYSTEMS (T-CNS), and IEEE TRANSACTIONS ON AUTOMATION SCIENCE AND ENGINEERING (T-ASE).